Imaging Science in Dentistry 2024; 54: 327-35
https://doi.org/10.5624/isd.20240061

Expression of beam hardening artifacts on horizontally stitched cone-beam computed tomography images

Juliana B Melo da Fonte[1], Rocharles Cavalcante Fontenele[2], Deborah Queiroz Freitas[3,*]

[1]*Department of Oral and Maxillofacial Radiology, UConn School of Dental Medicine, Farmington, CT, USA*
[2]*OMFS IMPATH Research Group, Department of Imaging and Pathology, Faculty of Medicine, KU Leuven, Leuven, Belgium*
[3]*Department of Oral Diagnosis, Division of Oral Radiology, Piracicaba Dental School, University of Campinas, Piracicaba, SP, Brazil*

ABSTRACT

Purpose: This study was performed to evaluate the expression of beam hardening artifacts generated by high atomic number materials in stitched cone-beam computed tomography (CBCT) images, compared to the traditional acquisition mode.

Materials and Methods: CBCT volumes were acquired using an acrylic resin phantom embedded with pairs of cylinders made from amalgam dental alloy, cobalt-chromium alloy, gutta-percha, titanium, and zirconium. These cylinders were placed within the overlapping zones of the stitching reconstruction area. For each material, 3 acquisitions were conducted: 1 utilizing the automatic stitching process with a FOV of 80×37 mm, and 2 with smaller FOVs of 50×37 mm. For the smaller FOVs, 1 scan targeted the anterior region, while the other focused on the left posterior region. Thus, 3 groups were formed: stitched FOV, anterior FOV, and posterior FOV. Artifact expression was assessed by calculating the means and standard deviations (SDs) of the gray values in 4 regions of interest located anteriorly, posteriorly, medially, and laterally to the cylinders. Analysis of variance was used to compare the data, with an alpha level of 5%.

Results: The stitched FOV exhibited lower SD values than the posterior and anterior FOVs ($P<0.05$). Regarding the materials evaluated, amalgam, cobalt-chromium, and zirconium generally demonstrated higher SDs of the gray values than gutta-percha and titanium ($P<0.05$).

Conclusion: Horizontally stitched CBCT images demonstrated lower artifact expression compared to the traditional mode of acquisition. ***(Imaging Sci Dent 2024; 54: 327-35)***

KEY WORDS: Cone-Beam Computed Tomography; Artifacts; Dental Materials

Introduction

A variety of cone-beam computed tomography (CBCT) scanners are available, featuring numerous field of view (FOV) sizes. These range from FOVs of small height and diameter to those capable of reconstructing the entire head and neck region.[1-4] While small to medium FOVs are sufficient for many dental indications and applications, certain cases, such as orthognathic surgery planning, necessitate a larger FOV. Acquiring images at these larger FOVs requires a correspondingly large detector, which can be costly. To mitigate the expense associated with larger detectors, some devices employ a technique known as multi-volume fusion, or stitching, to achieve larger FOVs.[1,3-5]

The stitching process can be performed either automatically or manually. Automatic stitching is possible in the vertical direction, as seen in the OP300 Maxio (KaVo Dental, Tuusula, Finland) and Planmeca Promax 3D Mid (Planmeca, Helsinki, Finland) systems, and in the horizontal direction, as utilized by the CS9000 3D (Carestream Health Inc, Rochester, NY, USA) and Planmeca Promax 3D Classic (Planmeca) systems. Notably, however, this method causes

This study was financed in part by the Coordenação de Aperfeiçoamento de Pessoal de Nível Superior - Brazil (CAPES) - Finance Code 001.
Received March 27, 2024; Revised July 26, 2024; Accepted August 2, 2024
Published online August 25, 2024
*Correspondence to : Prof. Deborah Queiroz Freitas
Department of Oral Diagnosis, Piracicaba Dental School, University of Campinas, Av. Limeira, 901, Areião, Zip-Code 13414-903, Piracicaba, SP, Brazil
Tel) 55-19-21065227, E-mail) deborahq@unicamp.br

certain regions to be captured twice, with overlap during reconstruction and a resulting duplication of the peripheral FOV regions at these locations.[3-6] Horizontal stitching begins with the acquisition of 3 sequential small FOVs. These images are then aligned using anatomical landmarks and automatically combined into a single, comprehensive 3-dimensional (3D) image. For this process to succeed, the patient must remain completely motionless throughout the entire image acquisition phase.[5-7]

Stitching can be performed manually, through visual recognition of specific anatomical features (InVivo Dental; Anatomage, San Jose, CA, USA), or automatically (as with Planmeca Romexis software), utilizing specific features of the CBCT system software. Studies have demonstrated the accuracy and reliability of stitching for conducting linear measurements.[5-8] However, the precise mechanisms by which CBCT software features execute the stitching reconstruction process remain unclear, specifically whether data from smaller acquisitions are overlapped and then added or subtracted.

Despite the quality and advantages that CBCT provides, it has some limitations. One of these is the production of artifacts, which can interfere with the diagnosis of various conditions by reducing image quality. Artifacts arise from a discrepancy between the physical acquisition process and the mathematical reconstruction of the image.[2,3,9] Among the types of artifacts generated in CBCT images, those resulting from the beam hardening effect are particularly detrimental to diagnosis.[9-11] These artifacts are caused by the presence of materials with a high atomic number, such as dental restorations, metal crowns, dental implants, gutta-percha, and metal pins, leading to the appearance of hypodense and hyperdense bands or streaks.[3,9,12,13]

Furthermore, the position of the object within the FOV is known to affect image quality. More artifacts tend to appear on CBCT images when an object is located at the periphery of the FOV rather than at the center.[13] This high artifact generation for peripheral objects may be attributed to the cone-shaped beam effect, where the divergence of the beam causes CBCT images to contain less information for peripherally located structures.[2]

Previous studies have analyzed the impact of an object's position within the FOV on image quality and the generation of artifacts.[14-16] However, to these authors' knowledge, no study has yet assessed the image quality and artifact generation associated with various high atomic number objects when placed in the peripheries—or doubly-scanned regions—of horizontally stitched images. It remains unclear whether the duplicate scanning of these zones alters artifact expression. Such an impact could reduce artifacts by providing additional information and thus aid the reconstruction process; alternatively, the superimposition of artifacts from 2 smaller FOVs might amplify the artifact expression in the final stitched image. Thus, this study aimed to evaluate the artifact expression caused by high atomic number materials on CBCT scans acquired with stitched images, compared to the traditional mode.

Methods and Materials

Sample preparation

A polymethyl methacrylate (PMMA) phantom, with perforations to mimic a lower dental arch, was utilized. This phantom measured 100 mm in diameter and 43.5 mm in height.[17] The study investigated 5 materials of high atomic number that are commonly used in dental practice: amalgam dental alloy (Southern Dental Industries Ltd, Bayswater, Australia), cobalt-chromium alloy (Scardua Laboratory, Vila Velha, Brazil), gutta-percha (Dentsply Sirona, Charlotte, USA), titanium (S.I.N. Implant System, Sao Paulo, Brazil), and zirconium (Scardua Laboratory).

The gutta-percha and amalgam cylinders were fabricated using a silicone condensation matrix (Zetaplus Denso; Zhermac, Badia Polesine, Italy) measuring 5.4 mm in height and 5.5 mm in diameter. Permite amalgam capsules, containing 47.9% mercury, were condensed within the matrix using a Ward Duflex condenser (SS White, Philadelphia, PA, USA) after being agitated for 8 seconds in an Ultramat 2 amalgamator (Southern Dental Industries Ltd). Odahcam gutta-percha sticks (Dentsply Sirona) were heated in an endodontic syringe to shape the cylinders. During the plastic phase, the softened gutta-percha was inserted into the matrix and compacted with a Paiva 22 presser (Golgran, Sao Caetano do Sul, Brazil). After 30 minutes, the amalgam and gutta-percha cylinder samples were removed from the matrix.

For the zirconium and cobalt-chromium cylinders, a computer-aided design/computer-aided manufacturing (CAD-CAM) system was utilized to mill them from a Standard Triangle Language (STL) file provided by Scardua Laboratory. The process began with the design of the cylinder using 3D CAD software to create precise digital models. Subsequently, CAM software generated toolpaths to guide the milling machine's cutting tools. Zirconium is typically milled in its softer pre-sintered state, which allows for higher milling speeds and the use of diamond-coated tools. Minimal cooling is employed to prevent contamination. In contrast, cobalt-chromium, a hard and durable material, requires milling at high spindle speeds with robust carbide

cutting tools and continuous coolant flow to prevent overheating and tool wear. Following the milling process, the cylinders were deburred to remove any sharp edges and polished to achieve the desired surface finish. A thorough inspection was conducted to ensure that they met the necessary specifications and tolerances. The titanium cylinders were supplied by S.I.N. Implant System.

Using a Discovery scale (OHAUS, Parsippany - Troy Hills, NJ, USA), the mass and density of each cylinder were determined in accordance with the Archimedes principle. Then, the volume of each cylinder was calculated (Table 1). To ensure high accuracy, these measurements were repeated 3 times.

Table 1. Compositions, atomic numbers, and densities of materials

Material	Atomic number (Z)	Density (g/cm^3)
Amalgam dental alloy	Mercury: 80; Silver: 47; Zinc: 30	10.9
Cobalt-chromium alloy	Cobalt: 24; Chromium: 27	7.8
Gutta-percha	Isoprene rubber/zinc oxide: 30	2.6
Titanium	22	6
Zirconium	40	6.1

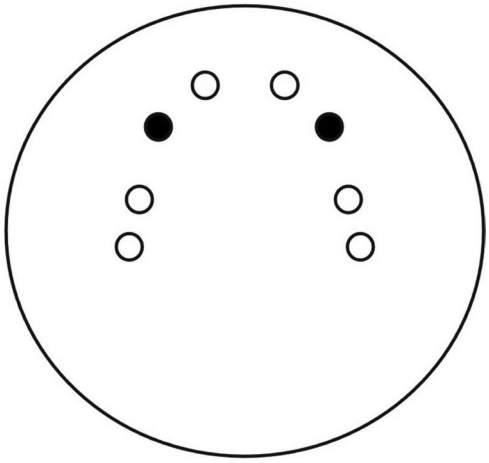

Fig. 1. An axial view of the phantom layout shows the positions of the cylinders (black circles).

Image acquisition

Two cylinders made of the same material were placed in designated slots within the phantom, positioning them within the overlapping zones of the stitching to simulate a clinical scenario involving multiple high-density materials (Fig. 1). The phantom was then situated on the platform of the CS9000 3D CBCT device, with settings of 70 kV, 10 mA, and a voxel size of 0.2 mm (Fig. 2). Utilizing the device's lights, the phantom was aligned in a manner akin to patient positioning for a scan of the entire mandible. Without moving the phantom, 3 scans were acquired for each pair of materials: 1 utilizing the automatic stitching reconstruction, with a FOV of 80 × 37 mm, and 2 additional scans with smaller FOVs of 50 × 37 mm. For the smaller FOVs, 1 scan targeted the anterior region, while the other focused on the left posterior region (Fig. 3). These specific positions for the small FOVs were selected to replicate the placement of the individual FOVs that comprise the stitched images. Consequently, 3 groups were established, termed the stitched FOV, anterior FOV, and posterior FOV.

Image evaluation

Images were imported into ImageJ v.1.51 (National Institutes of Health, Bethesda, MD, USA) for analysis. An oral

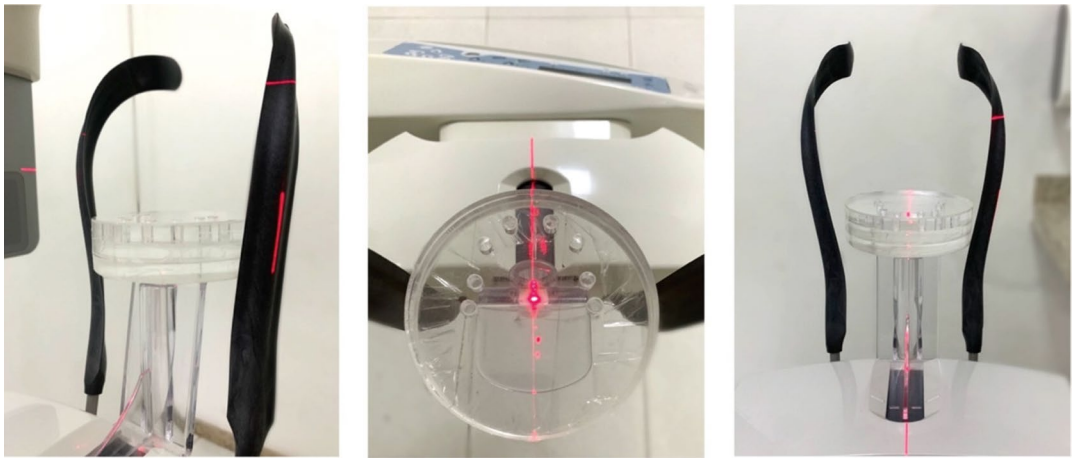

Fig. 2. Images of the phantom positioned on the tomography device (CS9000 3D; Carestream Health Inc, Rochester, NY, USA).

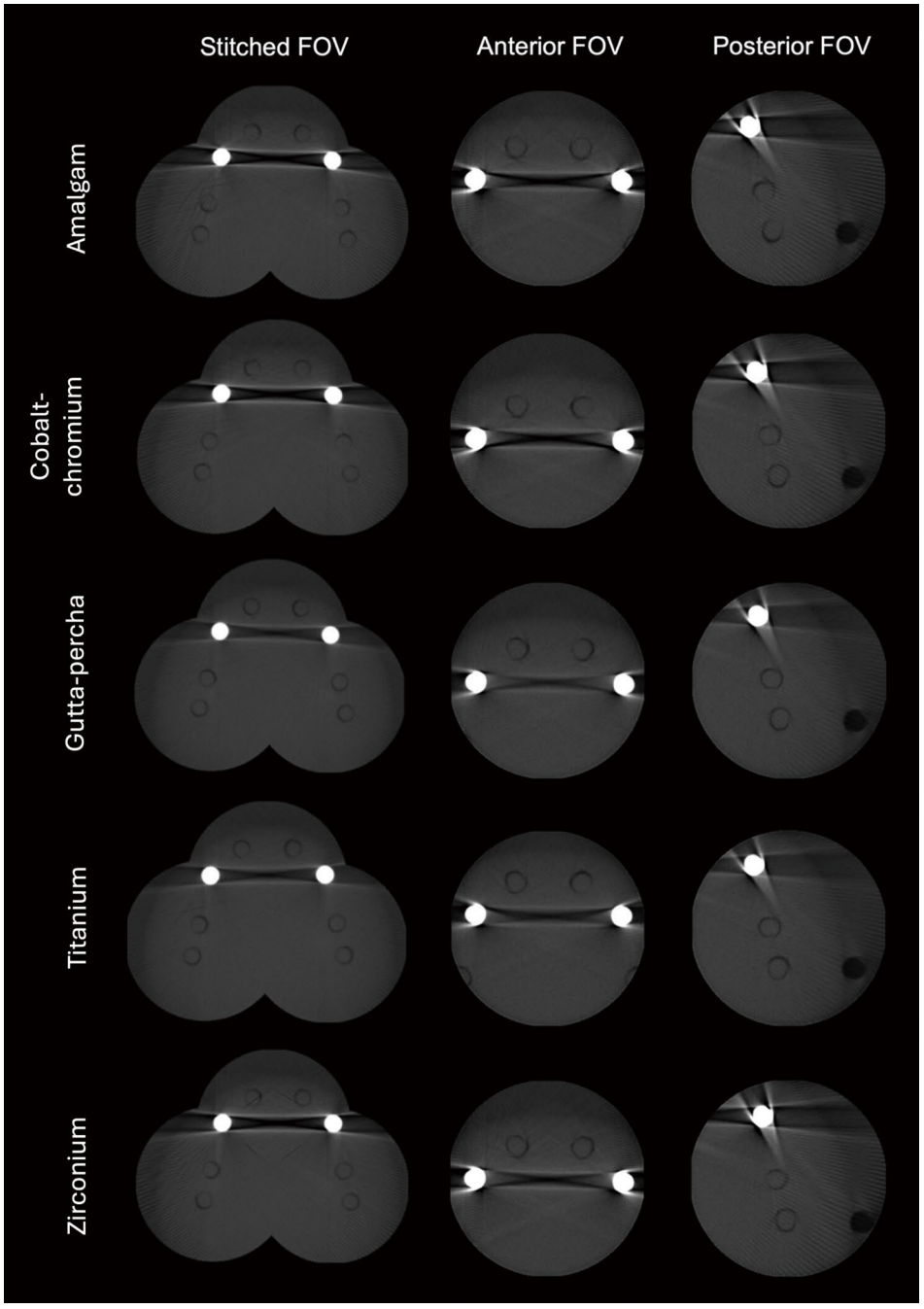

Fig. 3. Results of cone-beam computed tomography acquisitions for each material.

radiologist with 5 years of experience in CBCT evaluation assessed each image individually in a quiet, darkened room. Axial images were utilized to establish regions of interest (ROIs) and to standardize the analysis. The midpoint of the cylinder was determined by visual inspection: the axial reconstructions where the cylinder first and last appeared were identified, and the average of these points was calculated to define the cylinder's center. For the analysis of artifact expression, 4 rectangular ROIs were created around each cylinder. The ROIs placed medially and laterally measured 1×6 mm (width $\times$ height), while those positioned anteriorly and posteriorly measured 8×1 mm, as shown in Figure 4. These dimensions ensured that identical ROIs could be drawn around all cylinders, irrespective of their location within the FOV. The stitched and anterior FOVs included 2 cylinders; in these cases, only the left cylinder was evaluated, as it was the one present in the posterior FOV.

Artifact expression was assessed by calculating the mean and standard deviation (SD) of the gray values within the

ROIs. A higher mean gray value suggests a brighter area, whereas a higher SD value reflects larger variation in gray values, indicative of greater artifact production.

To increase the reliability of the analysis, mean and SD data for each ROI were collected at 3 levels of the cylinder: the center, 10 reconstructions above, and 10 below the central region. Thirty days after the initial evaluation, 30% of the sample was reassessed under the same conditions to determine the intra-examiner agreement.

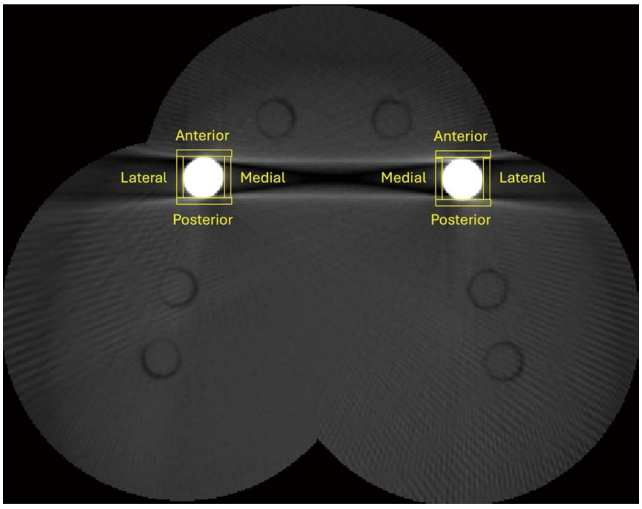

Fig. 4. Four regions of interest positioned around the cylinder for each field of view.

Statistical analysis

For data analysis, multi-way analysis of variance was employed to assess the effects of the factors under study: FOV, ROI, and material type. The intraclass correlation coefficient was used to evaluate intra-examiner agreement. All statistical analyses were performed using SPSS version 23.0 (IBM Corp., Armonk, NY, USA), with the significance threshold set at 5%. The power of the analysis, considering the results and the number of repetitions for each group, was determined to be 90%. The null hypothesis posited that FOV, ROI, and material type would not influence the mean and SD of the gray values.

Results

Table 2 summarizes the mean gray values according to the variables examined. Overall, the stitched FOV did not exhibit significantly different mean gray values compared to the anterior and posterior FOVs. Notable exceptions were observed for gutta-percha in the posterior, medial, and lateral ROIs, and for zirconium in the posterior and medial ROIs, where differences were statistically significant

Table 2. Gray values according to field of view (FOV), region of interest (ROI), and material

Material	FOV	ROI			
		Anterior	Posterior	Medial	Lateral
Amalgam dental alloy	Stitched	72.98 ± 4.09^{A}	87.49 ± 5.02^{A}	58.08 ± 1.61^{B}	45.06 ± 1.42^{B}
	Anterior	88.00 ± 7.60^{A}	$77.61 \pm 7.13^{AB*}$	67.30 ± 6.42^{B}	37.58 ± 1.16^{C}
	Posterior	71.70 ± 13.23^{A}	80.15 ± 12.15^{A}	74.99 ± 15.17^{A}	45.34 ± 8.78^{B}
Cobalt-chromium alloy	Stitched	70.73 ± 6.06^{A}	89.73 ± 9.94^{A}	57.01 ± 5.53^{B}	42.50 ± 3.11^{C}
	Anterior	83.36 ± 10.58^{B}	$107.66 \pm 6.60^{A\#}$	71.26 ± 0.52^{B}	28.68 ± 5.52^{C}
	Posterior	71.60 ± 11.04^{A}	88.70 ± 15.20^{A}	73.70 ± 14.49^{A}	36.33 ± 9.77^{B}
Gutta-percha	Stitched	62.41 ± 4.50^{AB}	76.97 ± 2.59^{Ab}	58.00 ± 1.21^{Bb}	53.76 ± 1.93^{Ba}
	Anterior	66.43 ± 6.60^{B}	92.24 ± 2.27^{Aa}	67.02 ± 0.70^{Bab}	39.21 ± 2.71^{Cb}
	Posterior	57.04 ± 9.04^{B}	75.14 ± 10.18^{Ab}	72.73 ± 15.12^{Aa}	49.17 ± 5.59^{Ba}
Titanium	Stitched	60.99 ± 1.36^{B}	81.59 ± 4.21^{A}	62.23 ± 2.33^{B}	50.22 ± 1.12^{B}
	Anterior	74.59 ± 4.79^{A}	$71.95 \pm 10.41^{A*}$	67.85 ± 2.84^{A}	41.47 ± 3.51^{B}
	Posterior	59.58 ± 8.91^{B}	76.33 ± 10.45^{A}	74.14 ± 11.38^{A}	45.88 ± 6.89^{B}
Zirconium	Stitched	79.98 ± 4.18^{A}	90.75 ± 4.86^{Aab}	61.35 ± 2.49^{ABb}	42.89 ± 1.39^{B}
	Anterior	84.31 ± 7.82^{B}	$103.59 \pm 4.07^{Aa\#}$	72.80 ± 1.34^{Bab}	36.67 ± 1.34^{C}
	Posterior	68.14 ± 11.20^{A}	84.60 ± 13.96^{Ab}	83.05 ± 16.13^{Aa}	42.89 ± 11.29^{B}

$P < 0.05$ for FOV, ROI, and material. Different capital letters denote significant differences between ROIs within the same material and FOV. In contrast, different lowercase letters signify significant differences between FOVs within the same ROI and material. Distinct symbols represent significant differences between materials within the same ROI and FOV.

Table 3. Standard deviations of gray values according to material, field of view (FOV), and region of interest (ROI)

Material	FOV	ROI			
		Anterior	Posterior	Medial	Lateral
Amalgam dental alloy	Stitched	$25.06 \pm 3.80^{Ab\#}$	$32.78 \pm 3.44^{Ab\#}$	$35.18 \pm 3.34^{Ab\#}$	$21.58 \pm 1.88^{Ab\#}$
	Anterior	$52.54 \pm 9.30^{Aa\#}$	$61.71 \pm 6.66^{Aa\#}$	$40.50 \pm 6.76^{Bb\#}$	$38.89 \pm 8.07^{Ba\#}$
	Posterior	$47.89 \pm 7.13^{Ba\#}$	53.70 ± 7.79^{Ba}	$69.50 \pm 10.02^{Aa\#}$	47.09 ± 2.85^{Ba}
Cobalt-chromium alloy	Stitched	18.44 ± 2.36^{Bb}	31.04 ± 10.65^{Ac}	$35.59 \pm 5.85^{Ab\#}$	$20.84 \pm 4.32^{Bb\#}$
	Anterior	$48.78 \pm 7.57^{Ba\#}$	$73.02 \pm 3.17^{Aa\#}$	$41.62 \pm 2.90^{Bb\#}$	$23.79 \pm 1.01^{Cb*}$
	Posterior	40.60 ± 5.69^{Ba}	58.25 ± 9.76^{Ab}	$71.79 \pm 10.14^{Aa\#}$	37.18 ± 2.89^{Ba}
Gutta-percha	Stitched	$10.88 \pm 2.09^{Ab*}$	$21.72 \pm 4.90^{Ac*}$	$16.28 \pm 1.18^{Ab*}$	15.44 ± 1.22^{Ab}
	Anterior	$25.00 \pm 6.80^{Ba*}$	$55.57 \pm 2.75^{Aa*}$	$24.33 \pm 4.16^{Bb*}$	$23.78 \pm 2.71^{Bab*}$
	Posterior	$26.36 \pm 5.11^{Ba*}$	41.01 ± 5.22^{Ab}	$40.43 \pm 10.59^{Aa*}$	27.19 ± 2.29^{Ba}
Titanium	Stitched	$9.34 \pm 0.55^{Bb*}$	26.32 ± 5.67^{Ab}	$22.07 \pm 0.78^{Ab*}$	$9.91 \pm 1.02^{Bb*}$
	Anterior	$29.83 \pm 5.90^{Ba*}$	$47.91 \pm 4.30^{Aa*}$	$22.92 \pm 5.15^{Bb*}$	$31.02 \pm 2.89^{Ba*}$
	Posterior	$29.34 \pm 5.03^{Ba*}$	42.55 ± 5.31^{Aa}	$45.61 \pm 7.76^{Aa*}$	31.03 ± 1.83^{Ba}
Zirconium	Stitched	$24.82 \pm 4.48^{Bb\#}$	$31.67 \pm 3.96^{ABc\#}$	$39.23 \pm 3.20^{Ab\#}$	$20.95 \pm 1.19^{Bb\#}$
	Anterior	$48.13 \pm 7.34^{Ba\#}$	$77.07 \pm 3.78^{Aa\#}$	$37.17 \pm 6.17^{Bb\#}$	$39.69 \pm 1.55^{Ba\#}$
	Posterior	40.29 ± 5.44^{Ca}	53.95 ± 9.40^{Bb}	$68.16 \pm 10.94^{Aa\#}$	37.70 ± 3.09^{Ca}

$P < 0.05$ for FOV, ROI, and material. Different capital letters denote significant differences between ROIs within the same material and FOV. In contrast, different lowercase letters signify significant differences between FOVs within the same ROI and material. Distinct symbols represent significant differences between materials within the same ROI and FOV.

($P < 0.05$). Specifically, in the posterior ROI, the anterior FOV exhibited higher mean gray values than both the posterior and stitched FOVs for gutta-percha and zirconium. In the medial ROI, the posterior FOV had a higher mean gray value than the stitched FOV for both materials. In the lateral ROI, the stitched and posterior FOVs demonstrated higher mean gray values than the anterior FOV for gutta-percha.

Regarding the effect of the ROI, the mean gray value was generally highest in the posterior ROI across all materials, followed by the anterior, medial, and lateral ROIs ($P < 0.05$).

The influence of the material on the mean gray values was noted solely in the posterior ROI within the anterior FOV. Here, cobalt-chromium and zirconium exhibited higher values than amalgam and titanium ($P < 0.05$). Gutta-percha demonstrated intermediate values, which did not differ significantly from those of the other materials.

Table 3 presents the average SDs of the gray values for the variables under investigation. Across all materials, the stitched FOV demonstrated lower SD values than both posterior and anterior FOVs ($P < 0.05$).

Regarding ROI, the posterior ROI exhibited the highest SD values for the anterior FOV, while the medial ROI displayed the highest SD values for the posterior FOV. In the case of the stitched FOV, the posterior and medial ROIs generally had the highest SDs, while the anterior and lateral ROIs had the lowest values ($P < 0.05$).

Among materials, amalgam, cobalt-chromium, and zirconium generally exhibited higher SD values than gutta-percha and titanium. The exception was the lateral ROI within the anterior FOV, in which cobalt-chromium demonstrated lower SD values ($P < 0.05$). The intra-examiner agreement was excellent, with an intraclass correlation coefficient of 1.0.

Discussion

Several studies have confirmed that stitching is an accurate, reliable, and stable method for performing linear measurements.[5-8] However, the literature includes scarce research examining the effect of stitching on artifact expression. To these authors' knowledge, this study is the first to objectively evaluate the image quality and artifact expression associated with the placement of high atomic number objects in the overlapping regions of stitched images. The findings offer insights into whether horizontally composed stitched images yield better image quality than smaller anterior and posterior FOVs, when an object is located at the periphery of the FOV.

Image stitching can be achieved using specific software features available in CBCT systems. However, the precise operation of these features in the stitching reconstruction

process remains unclear. It is uncertain whether data from smaller acquisitions are superimposed and then added together in some fashion, potentially providing additional information for reconstruction and reducing artifacts. Similarly, it is not known whether overlapping artifacts from 2 smaller FOVs intensify artifact expression in the final stitched image. The positioning of an object within the FOV has been demonstrated to substantially impact image quality. Previous studies have shown that objects located at the periphery of the FOV produce higher noise levels compared to objects positioned at the center.[14-16] This increased noise stems from the cone-beam effect observed on CBCT images, in which beam divergence causes less information to be provided about peripheral structures.[2] In stitched images, even when artifact-generating materials are in the periphery of the component FOVs (as simulated in the present study), more information is available because 2 scans of the region are acquired. Thus, these authors hypothesized that the stitched images might exhibit different artifact expression compared to the individual FOV. According to the results, the stitched FOV showed a lower SD of gray values relative to the anterior and posterior FOVs. Although the use of a smaller FOV has traditionally resulted in fewer artifacts than a larger field, the theory regarding the present research is that stitching acquisitions provide more information for image reconstruction, thus reducing artifact expression.

Consistent with previous research, the mean and SD of gray values within an ROI were calculated to objectively assess artifact production on CBCT images.[14,18-20] The mean gray value is used to evaluate the degree of darkening or brightening in an image. A higher mean gray value indicates a brighter image, and vice versa. In contrast, SD offers an estimation of image uniformity, which is affected by the presence of high-density materials, as reflected by the variation in gray values. Thus, a higher SD value—that is, larger variation—indicates greater artifact production.[20] In the present study, the mean gray values were generally highest for the posterior ROI, followed by the anterior, medial, and lateral ROIs. Regarding SD, the medial and posterior ROIs typically exhibited the highest SD values, while the lateral ROI had the lowest. These findings can be attributed to the position of the ROIs and the specific artifact patterns they represent. As illustrated in Figure 4, the anterior and posterior ROIs were situated in regions that appeared more hyperdense (higher values) than the areas covered by the medial and lateral ROIs. Additionally, the medial ROI sometimes included 1 or more hyperdense streaks along with a hypodense band, resulting in greater grayscale variation than the lateral ROI, which did not include hyperdense streaks. This pattern was also observed in the anterior and posterior ROIs for the anterior and posterior FOVs.

Subjectively, both anterior and posterior ROIs appeared to exhibit hyperdense streaks and hypodense bands with distinct patterns for each ROI, which were not observed in the stitched FOV. The subjective observation of fewer artifacts is also reflected in the gray values. However, interpreting decreases in gray values alone does not differentiate an increase in hypodense artifacts from a decrease in hyperdense artifacts. Accordingly, this analysis was supplemented with the SDs of grey values. Notably, the stitched FOV generally exhibited fewer artifacts, as evidenced by lower SD values compared to other FOVs. Thus, one can infer that lower values in certain posterior and medial ROIs are indicative of a reduction in hyperdense artifacts.

The appearance of both dark and bright bands in CBCT images is attributed to a phenomenon known as beam hardening. This occurs due to the polyenergy nature of the X-ray beam used in CBCT. When the beam passes through high-density materials, its average energy upon reaching the detector is higher than expected. This process alters the X-ray beam spectrum, leading to streaking artifacts in the image areas beyond the dense material. Additionally, photon starvation occurs when high-density materials absorb a meaningful portion of the X-ray beam, resulting in areas with a low photon count. This manifests as dark streaks or patches between 2 high-density materials in the CBCT images. Sometimes referred to as complete absorption or "starvation," this phenomenon occurs along specific beam paths where all photons are absorbed by the dense material, further complicating the interpretation of structures surrounding the high-density objects.[2,3,9,12,21,22] Since the present study utilized 2 cylinders of high-density materials for CBCT acquisitions, it is unsurprising that both phenomena were present and influenced the mean and SD results. These artifacts highlight the importance of understanding and mitigating their impact for accurate clinical interpretation of CBCT scans, particularly in dental and maxillofacial imaging.[18,21]

While not the objective of the present study, examination revealed that in both anterior and posterior FOV acquisitions, the cylinders appeared altered and/or distorted. This effect, known as volumetric change, volumetric distortion, or blooming, is commonly associated with high-density materials and results in the tomographic volume of an object appearing larger than its physical size.[2,18,23] Several factors contribute to this overestimation of object volume, including the CBCT system, technical parameters, and type of material scanned.[23] The current observations are consistent

with these phenomena, as evidenced by the higher SD values in the anterior and posterior FOVs relative to the stitched FOV. Nevertheless, further research is necessary to verify this volumetric distortion.

Regarding the effect of the material on SD, amalgam, cobalt-chromium and zirconium generally exhibited higher SD values than gutta-percha and titanium. The results can be ascribed to the relatively lower atomic numbers and densities of gutta-percha and titanium, as opposed to amalgam, cobalt-chromium, and zirconium. This is because higher atomic numbers and greater physical densities contribute to increased artifact expression.[24-26]

To compare stitched and non-stitched images, certain conditions were selected for acquiring scans and simulating artifact formation, such as employing 2 cylinders. Furthermore, a single acquisition parameter was chosen to minimize the introduction of additional confounding factors. Importantly, altering these conditions—for instance, using 1 cylinder instead of 2, or modifying the energy parameters or spatial resolution—could yield different results. However, the present objective was not to evaluate the impact of the number of cylinders or acquisition parameters on artifact expression, as these variables have been previously investigated.[10,11,27] Furthermore, using only one cylinder did not result in a reconstructed stitched image, likely due to insufficient information in one of the overlapping areas.

Several authors have employed a variety of techniques to simulate *in vivo* conditions, such as geometric phantoms, dry skulls, and patient image databases, to assess the effects of artifacts on image quality, measurement accuracy, and reliability.[10,14,28-30] As this study represents a pioneering effort in *in vitro* research, a controlled and homogeneous environment was essential. Therefore, a lower dental arch was simulated using a PMMA phantom. This setup, free from the confounding attenuation effects of other structures, enabled the quantification of artifacts arising specifically from cylinders with a high atomic number.[14,31] Further research is needed to understand how stitched images influence image interpretation and clinical utility.

Although future studies are necessary to clarify this study's clinical significance, it rests in the potential for improved image quality with stitched CBCT scans. When indicated, clinicians may benefit from clearer visualization of anatomical structures and pathology when utilizing a CBCT unit equipped with this feature. This enhancement may aid in diagnosis, treatment planning, and evaluation of treatment outcomes, particularly in patients with high-density dental materials in the region where the smaller FOVs are merged to form the stitched FOV. However, the application of stitched CBCT scans must be clinically justified, as their use entails a higher radiation dose for the patient.

In conclusion, compared to traditional acquisition, stitched CBCT images display reduced artifact expression. Professionals should recognize this potential benefit of stitched CBCT images.

Conflicts of Interest: None

Acknowledgments

The authors extend their gratitude to S.I.N. Implant System (São Paulo, Brazil) for supplying the titanium cylinders and to Fernanda Coelho-Silva for providing the additional cylinders.

References

1. Scarfe WC, Li Z, Aboelmaaty W, Scott SA, Farman AG. Maxillofacial cone beam computed tomography: essence, elements, and steps to interpretation. Aust Dent J 2012; 57 Suppl 1: 46-60.
2. Scarfe WC, Farman AG. What is cone-beam ct and how does it work? Dent Clin North Am 2008; 52: 707-30.
3. Pauwels R, Araki K, Siewerdsen JH, Thongvigitmanee SS. Technical aspects of dental CBCT: state of the art. Dentomaxillofac Radiol 2015; 44: 20140224.
4. Gaêta-Araujo H, Alzoubi T, Vasconcelos KF, Orhan K, Pauwels R, Casselman JW, et al. Cone beam computed tomography in dentomaxillofacial radiology: a two-decade overview. Dentomaxillofac Radiol 2020; 49: 20200145.
5. Kopp S, Ottl P. Dimensional stability in composite cone beam computed tomography. Dentomaxillofac Radiol 2010; 39: 512-6.
6. Egbert N, Cagna DR, Ahuja S, Wicks RA. Accuracy and reliability of stitched cone-beam computed tomography images. Imaging Sci Dent 2015; 45: 41-7.
7. Kim MK, Kang SH, Lee EH, Lee SH, Park W. Accuracy and validity of stitching sectional cone beam computed tomographic images. J Craniofac Surg 2012; 23: 1071-6.
8. Srimawong P, Krisanachinda A, Chindasombatjaroen J. Accuracy of linear measurements in stitched versus non-stitched cone beam CT images. CU Dent J 2015; 38: 93-104.
9. Schulze R, Heil U, Gross D, Bruellmann DD, Dranischnikow E, Schwanecke U, et al. Artefacts in CBCT: a review. Dentomaxillofac Radiol 2011; 40: 265-73.
10. Vasconcelos TV, Bechara BB, McMahan CA, Freitas DQ, Noujeim M. Evaluation of artifacts generated by zirconium implants in cone-beam computed tomography images. Oral Surg Oral Med Oral Pathol Oral Radiol 2017; 123: 265-72.
11. Gaêta-Araujo H, Nascimento EH, Fontenele RC, Mancini AX, Freitas DQ, Oliveira-Santos C. Magnitude of beam-hardening artifacts produced by gutta-percha and metal posts on cone-beam computed tomography with varying tube current. Imaging Sci Dent 2020; 50: 1-7.
12. Pauwels R, Stamatakis H, Bosmans H, Bogaerts R, Jacobs R, Horner K, et al. Quantification of metal artifacts on cone beam

computed tomography images. Clin Oral Implants Res 2013; 24 Suppl A100: 94-9.
13. Parsa A, Ibrahim N, Hassan B, Syriopoulos K, van der Stelt P. Assessment of metal artifact reduction around dental titanium implants in cone beam CT. Dentomaxillofac Radiol 2014; 43: 20140019.
14. Queiroz PM, Santaella GM, da Paz TD, Freitas DQ. Evaluation of a metal artifact reduction tool on different positions of a metal object in the FOV. Dentomaxillofac Radiol 2017; 46: 20160366.
15. Pauwels R, Jacobs R, Bogaerts R, Bosmans H, Panmekiate S. Reduction of scatter-induced image noise in cone beam computed tomography: effect of field of view size and position. Oral Surg Oral Med Oral Pathol Oral Radiol 2016; 121: 188-95.
16. Taylor C. Evaluation of the effects of positioning and configuration on contrast-to-noise ratio in the quality control of a 3D Accuitomo 170 dental CBCT system. Dentomaxillofac Radiol 2016; 45: 20150430.
17. Martins LA, Queiroz PM, Nejaim Y, Vasconcelos KF, Groppo FC, Haiter-Neto F. Evaluation of metal artifacts for two CBCT devices with a new dental arch phantom. Dentomaxillofac Radiol 2020; 49: 20190385.
18. Codari M, de Faria Vasconcelos K, Ferreira Pinheiro Nicolielo L, Haiter Neto F, Jacobs R. Quantitative evaluation of metal artifacts using different CBCT devices, high-density materials and field of views. Clin Oral Implants Res 2017; 28: 1509-14.
19. Fontenele RC, Nascimento EH, Vasconcelos TV, Noujeim M, Freitas DQ. Magnitude of cone beam CT image artifacts related to zirconium and titanium implants: impact on image quality. Dentomaxillofac Radiol 2018; 47: 20180021.
20. Min CK, Kim KA. Reducing metal artifacts between implants in cone-beam CT by adjusting angular position of the subject. Oral Radiol 2021; 37: 385-94.
21. Mori I, Machida Y, Osanai M, Iinuma K. Photon starvation artifacts of X-ray CT: their true cause and a solution. Radiol Phys Technol 2013; 6: 130-41.
22. Brüllmann D, Schulze RK. Spatial resolution in CBCT machines for dental/maxillofacial applications - what do we know today? Dentomaxillofac Radiol 2015; 44: 20140204.
23. Vasconcelos KF, Nicolielo LF, Nascimento MC, Haiter-Neto F, Bóscolo FN, Van Dessel J, et al. Artefact expression associated with several cone-beam computed tomographic machines when imaging root filled teeth. Int Endod J 2015; 48: 994-1000.
24. Coelho-Silva F, Martins LA, Braga DA, Zandonade E, Haiter-Neto F, de-Azevedo-Vaz SL. Influence of windowing and metal artefact reduction algorithms on the volumetric dimensions of five different high-density materials: a cone-beam CT study. Dentomaxillofac Radiol 2020; 49: 20200039.
25. Costa ED, Brasil DM, Queiroz PM, Verner FS, Junqueira RB, Freitas DQ. Use of the metal artefact reduction tool in the identification of fractured endodontic instruments in cone-beam computed tomography. Int Endod J 2020; 53: 506-12.
26. de-Azevedo-Vaz SL, Peyneau PD, Ramirez-Sotelo LR, Vasconcelos Kde F, Campos PS, Haiter-Neto F. Efficacy of a cone beam computed tomography metal artifact reduction algorithm for the detection of peri-implant fenestrations and dehiscences. Oral Surg Oral Med Oral Pathol Oral Radiol 2016; 121: 550-6.
27. Oliveira ML, Freitas DQ, Ambrosano GM, Haiter-Neto F. Influence of exposure factors on the variability of CBCT voxel values: a phantom study. Dentomaxillofac Radiol 2014; 43: 20140128.
28. Van Dessel J, Nicolielo LF, Huang Y, Slagmolen P, Politis C, Lambrichts I, et al. Quantification of bone quality using different cone beam computed tomography devices: accuracy assessment for edentulous human mandibles. Eur J Oral Implantol 2016; 9: 411-24.
29. Jacobs R, Salmon B, Codari M, Hassan B, Bornstein MM. Cone beam computed tomography in implant dentistry: recommendations for clinical use. BMC Oral Health 2018; 18: 88.
30. Cremonini CC, Dumas M, Pannuti CM, Neto JB, Cavalcanti MG, Lima LA. Assessment of linear measurements of bone for implant sites in the presence of metallic artifacts using cone beam computed tomography and multislice computed tomography. Int J Oral Maxillofac Surg 2011: 40: 845-50.
31. Bamba J, Araki K, Endo A, Okano T. Image quality assessment of three cone beam CT machines using the SEDENTEXCT CT phantom. Dentomaxillofac Radiol 2013; 42: 20120445.